Supplemental Material for: Dirac Spin Liquid on the Spin-1/2 Triangular Heisenberg Antiferromagnet

Shijie Hu,[1,*] W. Zhu,[2,†] Sebastian Eggert,[1] and Yin-Chen He[3,‡]

[1] *Department of Physics and Research Center Optimas, Technische Universitat Kaiserslautern, 67663 Kaiserslautern, Germany*
[2] *Institute of Natural Sciences, Westlake Institute of Advanced Study, School of Science, Westlake University, Hangzhou, 030024, P. R. China*
[3] *Perimeter Institute for Theoretical Physics, Waterloo, Ontario N2L 2Y5, Canada*

In the Supplemental Material we present details related to mean-field theory of the Dirac spin liquid, the numerical procedure, and more supporting data. First of all, we restate the low energy theory for $N_f = 4$ QED$_3$ of the $U(1)$ Dirac spin liquid on the triangular lattice as well as its finite size effect on different geometries. Secondly, we discuss the numerical observations of even/odd sector states and weak nematic ordering of the groundstate. At last, we show additional data of transfer-matrix spectrum, entanglement entropy and gaps for total simulated 16 different geometries and/or system sizes.

$U(1)$ DIRAC SPIN LIQUID ON THE TRIANGULAR LATTICE

We fractionalize spin operators into fermionic partons, $\boldsymbol{S} = \boldsymbol{f}^\dagger \boldsymbol{\sigma} f$, $\boldsymbol{f}^\dagger = (f_\uparrow^\dagger, f_\downarrow^\dagger)$. The $U(1)$ Dirac spin liquid (DSL) can be described by a mean-field ansatz,

$$H_{MF} = -\sum_{\langle ij \rangle} \sum_{\sigma=\uparrow/\downarrow} [(-1)^{s_{ij}} f_{i,\sigma}^\dagger f_{j,\sigma} + h.c.]. \qquad (1)$$

$(-1)^{s_{ij}}$ is chosen to give a $\pi/0$ flux on the up/down triangles. One can find a band structure of two Dirac cones in the 1st Brillouin zone. Therefore, the low-energy theory of this state is described by $N_f = 4$ QED$_3$.

Once we put $U(1)$ DSL on a finite-width and infinite-length cylinder, there are several subtle finite size effects, which can be understood in the mean-field theory. First, the cylinder may trap an extra flux $\phi = 0$ or π from the emergent $U(1)$ gauge field [1]. The value of ϕ will be energetically determined. Second, we note that there is an even-odd effect for the mean-field ansatz. As shown in Fig. S1, cylinders with even and odd circumference L_y should have different gauge configurations. Next, we solve band structure with an additional phase $e^{i\sigma\theta/2+i\phi}$ for the hoppings across the boundary in axis $\boldsymbol{a}_1$, where θ is the external Aharonov-Bohm flux inserted in the cylinder and the factor $\sigma/2$ is due to that $f_{\uparrow/\downarrow}$ carries $\pm 1/2$ spin. So on the YCL_y-n cylinders, the properties of the band structure can be classified according to the even or oddness of L_y and n. If both L_y and n are even, $\phi = \pi$ will be energetically favored, and the fermions become gapless when $\theta = 2\pi$. For the other cases, the system behaves qualitatively similar no matter $\phi = 0$ or π, and the fermions will become gapless at $\theta = \pi$ or 3π, where only two (instead of four in the thermodynamic limit) Dirac fermions become gapless.

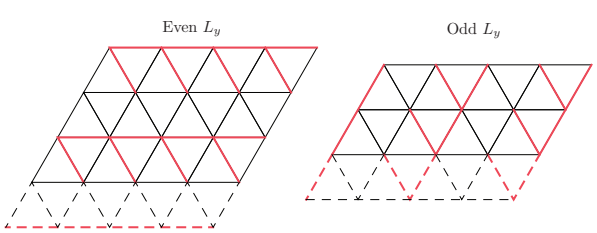

FIG. S1. $U(1)$ Dirac spin liquid ansatz on the cylindrical geometry with even/odd width L_y. We have hopping amplitude -1 on the red bond, 1 on the black bond.

TRANSFER MATRIX TECHNIQUE

In this section, we provide more details of the transfer matrix technique. In iDMRG, we wrap a 2D lattice on a thin cylinder with a finite circumference L_y but an infinite length L_x and use the snake-chain matrix product state (MPS) to cover the cylinder as shown in Fig. S2 (b) (for simplicity we view triangular lattice as a square lattice with a diagonal bond). Generically the snake-chain MPS geometry breaks the lattice translation symmetry along the a_1 direction, so we need to use $2n$ distinct matrices A_l ($l = 1, \cdots, 2n$) in the MPS of YC$2n$-0 cylinders (see Fig. S2 (b), left panel), while $4n+2$ matrices for YC$(2n+1)$-0 cylinder. For a special geometry, i.e. YCL_y-1, MPS recover two-site repeating structure, namely A_1-A_2, independent if L_y is even or odd (see Fig. S2 (b), right panel). On the other hand, the MPS is translation invariant and repeating along the direction a_2. Then, one can use the smallest repeating unit cell to define the transfer matrix (TM), as shown in Fig. S2 (c). The eigenvalues $\lambda_j = e^{ik_j - \xi_j^{-1}}$ of TM–$\mathbf{T}$ contain information of the correlation functions of all operators, which are further related to excitations of the system [2]. Physically, each eigenvalue corresponds to one excitation mode of the system: ξ_j gives the correlation length (or equivalently the inverse of gap), while k_j gives the momentum along the infinite direction of the

cylinder.

We can further extract the conserved quantum number of each excitation mode from TM. We note that the Schmidt basis (virtual index) of MPS has a well defined conserved quantum number (Q^α), hence each eigenvector of TM–$\mathbf{T}$ shall have a quantum number $Q = Q^\alpha - Q^{\alpha'}$ (Fig. S2(c)). From this calculation we can get the correlation-length spectrum of different S^z sectors. Below we discuss the method of calculating momentum (k_1, k_2) of the correlation length spectrum.

For the YCL_y-0 geometry, k_2 is nothing but k from the eigenvalues ($e^{ik-\xi^{-1}}$) of TM–$\mathbf{T}$, k_1 on the other hand requires a bit more work. Due to the snake covering the MPS does not have translational invariance along the compactified direction ($\mathbf{a_1}$). However, the Hamiltonian still has translational invariance along $\mathbf{a_1}$, hence the momentum k_1 is a conserved quantum number. In other words, k_1 is similar to other conserved quantum number (e.g. S^z) even though it is not encoded in MPS explicitly. To extract k_1 of each mode one needs to first obtain the conserved momentum k_1 of each Schmidt basis of the MPS using the mixed transfer matrix TM–$\mathbf{T}[T_1^{(y)}]$. The mixed TM–$\mathbf{T}[T_1^{(y)}]$ is pictorially defined in Fig. S2(d), namely it is defined by translating the MPS by one site along the $\mathbf{a_1}$ direction. Due to the translation invariance (along $\mathbf{a_1}$) the dominant eigenvector of $\mathbf{T}[T_1^{(y)}]$ should be $\mathbf{V}_{\alpha,\alpha'} = \delta_{\alpha,\alpha'} e^{i\mathbf{k}^\alpha}$, with $\mathbf{k}^\alpha$ being the conserved momentum k_1 of each Schmidt basis of the MPS. At last, each mode has the momentum $k_1 = \mathbf{k}^\alpha - \mathbf{k}^{\alpha'}$, where α and α' are the Schmidt basis of eigenvectors of TM–$\mathbf{T}$. In the simulation we inserted a finite flux θ in the cylinder, so the aforementioned momentum is further modified $(k_1 + \theta/L_y, k_2)$ to obtain the final correlation spectrum presented in the paper.

For the special geometry YCL_y-1, the momenta k_1 and k_2 are intertwined together. A benefit is that the MPS with snake-geometry is actually invariant under two-sites translation. And the momentum (k_1, k_2) can be obtained directly form the TM's eigenvalues $e^{ik-1/\xi}$,

$$2k_1 = k + 2\theta/L_y, \quad k_2 = kL_y/2. \tag{2}$$

Therefore, for the -1 geometry, one can still get k_1 and k_2, but k_1 has a π ambiguity.

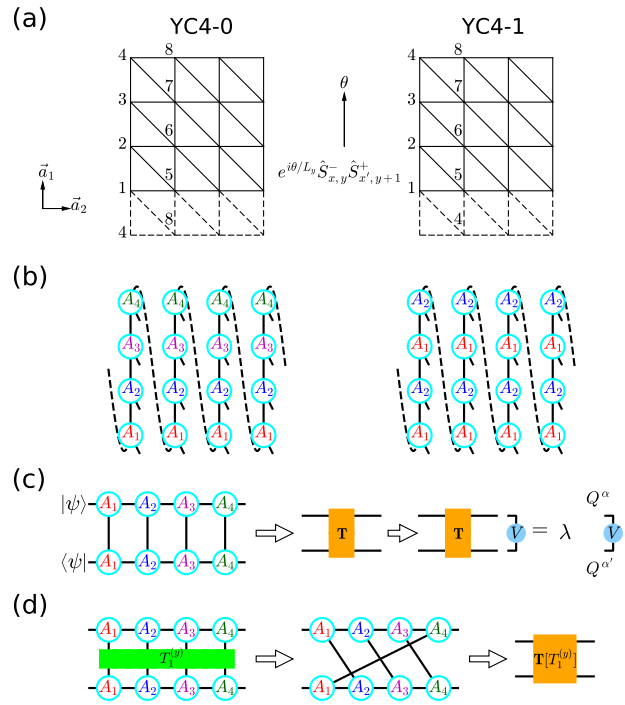

FIG. S2. (a) Equivalent square-lattice geometry for cylinders YC4-0 and YC4-1 on the triangular lattice. Bravais lattice primitive vectors $\mathbf{a}_{1/2}$ are indeed x/y axes. Inserted flux θ leads to a phase $e^{i\theta/L_y}$ in front of the spin-flipping term $\hat{S}^-_{x,y}\hat{S}^+_{x',y+1}$. (b) MPS representations for cylinders YC4-0 and YC4-1. (c) Pure transfer-matrix $\mathbf{T}$ of a smallest repeating unit cell. Its eigenvalues are determined by the quantum number discrepancy $q = Q^\alpha - Q^{\alpha'}$. (d) The mixed transfer matrix $\mathbf{T}[T_1^{(y)}]$ within a translation operation $T_1^{(y)}$ under one site along the cylinder circumference to calculate the momentum k_1 of each Schmidt basis.

EVEN/ODD-SECTOR STATES

It is well known that a topological ordered state has a number of topological degenerate groundstates once it is placed on a torus or an infinite cylinder (e.g. see [3]). Physically all topological sectors can be understood as a state with gauge fluxes and/or gauge charge lines (i.e. anyon lines) threaded in the torus or cylinder. Similarly the $U(1)$ DSL also has different groundstate sectors, which we will call as super-selection sectors instead of topological sectors. The properties of super-selection sectors of $U(1)$ DSL are not well understood theoretically, and it will not be pursued here either. In this section we will try to clarify some confusion regarding the topological/super-selection sectors obtained in DMRG simulations.

For a spin liquid Hamiltonian, DMRG simulations may yield several different "groundstates" (They are local minima of the Hamiltonian). However, there is no a-priori knowledge that these "groundstates" are different topological/super-selection sectors of a spin liquid phase. One has to conduct a thorough study on these "groundstates". For example, for a gapped topological spin liquid one needs to check if the modular matrix calculated from these "groundstates" agrees with the theoretical expectation for a topologically ordered phase. Otherwise one cannot exclude the possibility that different "groundstates" are the groundstates of different competing phases.

For the J_1-J_2 triangular spin liquid, one can obtain two "groundstates" on the YC2n-0 geometry. Previous

works [4–7] call these two "groundstates" the even and odd sectors, which pictorially corresponds to the number of valence bonds which cross a cut through the system. Their entanglement spectrum is one-fold or two-fold degenerate respectively, related to whether the $SO(3)$ spin rotation symmetry is realized projectively (two-fold) or not (one-fold). Numerically, we can get even/odd-sector states in the model without/with a pair of blank sites center-symmetrically located at two edge-columns during iDMRG "warming-up" steps. For three cylindrical geometries (YC$2n$-$(2k+1)$, YC$(2n+1)$-$2k$, YC$(2n+1)$-$(2k+1)$) there is no distinction between the even and odd sector, as these two sectors are simply related by a translation symmetry. In contrast, on the YC$2n$-$2k$ cylinders the odd sector and even sector are different states, and we mostly focus on the odd sector for this geometry. The even sector on the YC$2n$-$2k$ cylinders has a smaller gap, which also shows signatures of $U(1)$ DSL in the correlation length spectrum.

We remark that a parallel work [8] reported a large central charge $c = 5$ for the even sector state on a finite YC8-0 cylinder with a small length L_x. However, our data of the even sector state on YC8-0 cylinder does not agree with their observation. We use $SU(2)$-iDMRG and have simulated bond dimension up to $m^\star = 8192$ (equivalent to $U(1)$-DMRG with $m = 32014$). In Fig. S3, we fit the central using three different methods [9], namely the scaling of entropy with (a) the correlation length, (b) the $SU(2)$-DMRG bond dimension, and (c) the equivalent $U(1)$-DMRG bond dimension. The fitted central charge is much smaller than $c = 5$, and it keeps on decreasing as bond dimension increases. The central charge is likely to eventually go to $c = 0$ at the infinite bond dimension. So the observation of $c = 5$ in Ref. [8] might be a finite size effect: They only simulated a small cylinder ($L_x = 16$), but the central charge is only well defined in the 1D limit with $L_x \gg L_y = 8$.

We also note that there is a weak (C_6 breaking) nematic ordering in the spin liquid groundstates, namely a small difference of bond strengths in three inequal directions. The cylindrical geometry of DMRG breaks C_6 symmetry explicitly, so it is not surprising that a gapless $U(1)$ Dirac spin liquid weakly breaks C_6 [10]. Second, the C_6 breaking is weak and it becomes even weaker as we increase the bond dimension (Tab. I). The YC6-0 cylinder has extremely tiny nematicity, which may come from the fact that DMRG simulation is fully converged for such a small L_y.

TABLE I. Discrepancy of bond strengths (subtracted by the average value ~ -0.18) in the lowest-energy odd-sector state for various YCL_y-0 cylinders by setting $J_2/J_1 = 0.12$ and $\theta = 0$. They are shown in three inequal directions $\boldsymbol{a}_2$, $\boldsymbol{a}_1$ and $\boldsymbol{a}_1 - \boldsymbol{a}_2$. The data is accurate to 4 decimal places.

Geometry	m	$\boldsymbol{a}_2$	$\boldsymbol{a}_1$	$\boldsymbol{a}_1 - \boldsymbol{a}_2$
YC6-0	1024	0.0002	−0.0004	0.0002
	2048	−0.0004	0.0007	−0.0004
	4096	−0.0005	0.0011	−0.0005
	6144	−0.0006	0.0012	−0.0006
YC8-0	1024	0.0286	−0.0576	0.0290
	2048	0.0251	−0.0503	0.0252
	4096	0.0227	−0.0455	0.0227
	6144	0.0218	−0.0437	0.0219
	8192	0.0214	−0.0428	0.0214
	12288	0.0210	−0.0419	0.0210
YC10-0	1024	0.0517	−0.1072	0.0555
	2048	0.0459	−0.0927	0.0468
	4096	0.0404	−0.0818	0.0413
	6144	0.0381	−0.0765	0.0384
	8192	0.0365	−0.0732	0.0368
YC12-0	1024	0.0682	−0.1481	0.0798
	2048	0.0623	−0.1319	0.0696
	4096	0.0573	−0.1171	0.0598
	6144	0.0534	−0.1093	0.0559
	8192	0.0509	−0.1042	0.0533

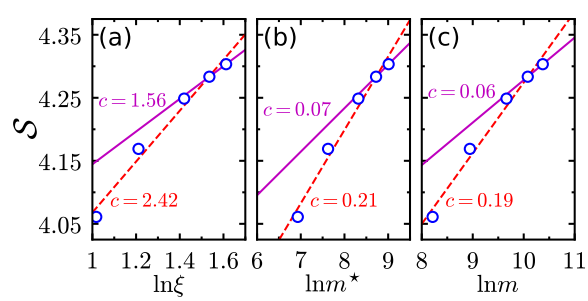

FIG. S3. Fitting the central charge of the even sector state on the YC8-0 cylinder. We use $SU(2)$-iDMRG and central charge is obtained by fitting entanglement entropy with (a) the largest correlation length $\ln\xi$, $\mathcal{S} = (c/6)\ln\xi + a$; (b) number of $SU(2)$ bases $m^\star$, $\mathcal{S} = 1/(\sqrt{12/c}+1)\ln m^\star + b^\star$; and (c) number of $U(1)$ bases m, $\mathcal{S} = 1/(\sqrt{12/c}+1)\ln m + b$. The five data points correspond to $SU(2)$ bond dimensions $m^\star = 1024$, 2048, 4096, 6144 and 8192. Maximal equivalent-$U(1)$ bond dimension $m = 32014$. Fitting with five points leads to red dashed lines while fitting with two largest points gives us magenta solid ones.

ADDITIONAL NUMERICAL DATA

Correlation length spectrum

We have in total simulated 16 different geometries and/or system sizes. Similar to the 4 clusters shown

in main text, the fermion bilinear and monopole operators also show up in correlation length spectrum of all the other 12 clusters. Here provide these data in this appendix.

$YC2n$-$(2k+1)$

Let us first look at the YC$2n$-$(2k+1)$ cylinder. We have already shown results of YC8-1 and YC10-1 cylinders in the main text, but for comparison we still plot them together with YC6-1 and YC12-1 ones in Fig. S4. For YC6-1 in the panel (a), we can insert the flux adiabatically until the flux $\theta > 0.3\pi$. Once a Dirac spin liquid is put on a small cylinder, it might have an instability by spontaneously generating massive terms during flux insertion. Therefore sometimes the numerical adiabatic change breaks down, but such finite size effect will be gone in the pure 2+1D limit, so only data is shown where the ground state remains in the spin liquid state. This is consistent with our observation that, for a larger system size (i.e. YC8-1, YC10-1 and YC12-1), the adiabatic twist can be maintained even when $\theta = \pi$. The trend of the spectrum is similar to larger system sizes, although the information of $\theta \in (0, 0.3\pi)$ is not enough for us to mark the type of its excitations. For other three cylinders, we also find one Dirac cone (low-lying excitations) is at a M point $(2k_1, k_2) = (0, \pi)$ (M_2 or M_3 point) and the other is close to the $K_\pm$ point $(2k_1, k_2) = \pm(2\pi/3, 2\pi/3)$. The former correspond to Fermion bilinears and the latter correspond to monopole operators.

Comparing the correlation length spectrum of various $L_y = 8$, 10 and 12, it seems that the larger the system is, the higher the Dirac mode (blue ⬡) is. We think it is an artifact from the finite entanglement effect (bond dimensions) in iDMRG simulations. For larger system sizes (L_y), the gapless modes suffers more severe truncation error, yielding a smaller correlation length at a given bond dimension. This artifact can be seen in Fig. S5, where clearly the Dirac mode becomes lower as the bond dimension increases. On the other hand, to achieve the same accuracy (truncation error), the required bond dimension increases exponentially with the circumference of the

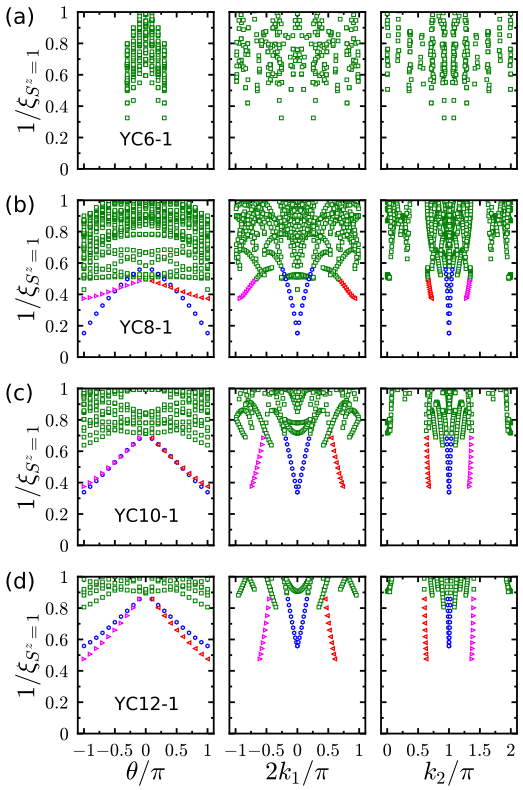

FIG. S4. Inverse correlation length $1/\xi_{S^z=1}$ (green □) as a function of the flux θ (left column), momentum $2k_1/\pi$ (middle column) and momentum k_2/π (right column) for YCL_y-1 cylinders by setting $J_2/J_1 = 0.12$. We choose bond dimension (a) $m = 4096$ for $L_y = 6$, (b) 12288 for $L_y = 8$, (c) 12288 for $L_y = 10$ and (d) 12288 for $L_y = 12$ respectively. Specially, we denote the lowest-lying spinon-pair excitations by blue ⬡ and monopole excitations by red ◁ and magenta ▷.

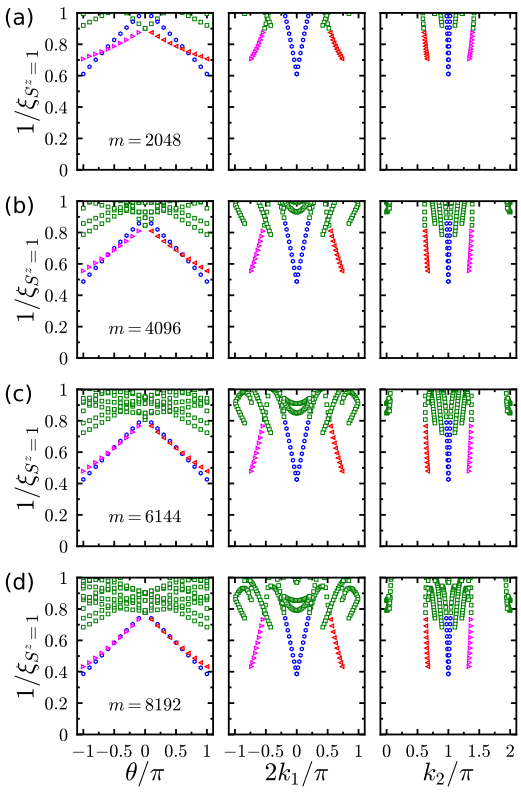

FIG. S5. Inverse correlation length $1/\xi_{S^z=1}$ (green □) as a function of the flux θ (left column), momentum $2k_1/\pi$ (middle column) and momentum k_2/π (right column) for YC10-1 cylinders by setting $J_2/J_1 = 0.12$. Bond dimension (a) $m = 2048$, (b) 4096, (c) 6144 and (d) 8192 respectively. Specially, we denote the lowest-lying spinon-pair excitations by blue ⬡ and monopole excitations by red ◁ and magenta ▷.

cylinder. Table II shows the truncation error for different bond dimensions, system sizes and flux. For the large system size (YC10-1, YC12-1), $m = 12288$ roughly gives comparable accuracy as $m = 1024$ for YC8-1. Therefore, more care should be taken if one wants to compare the results between different system sizes.

TABLE II. Truncation error for various YC2n-1 cylinder by setting $J_2/J_1 = 0.12$. $\theta = \pi$ has much bigger truncation error than $\theta = 0$.

	$m = 1024$	$m = 6144$	$m = 12288$
YC8-1 ($\theta = 0$)	5.3×10^{-5}	5.3×10^{-6}	1.7×10^{-6}
YC8-1 ($\theta = \pi$)	6.5×10^{-5}	1.1×10^{-5}	4.5×10^{-6}
YC10-1 ($\theta = 0$)	1.3×10^{-4}	2.5×10^{-5}	1.3×10^{-5}
YC10-1 ($\theta = \pi$)	1.5×10^{-4}	3.7×10^{-5}	2.1×10^{-5}
YC12-1 ($\theta = 0$)		5.8×10^{-5}	3.4×10^{-5}
YC12-1 ($\theta = \pi$)		7.1×10^{-5}	4.4×10^{-5}

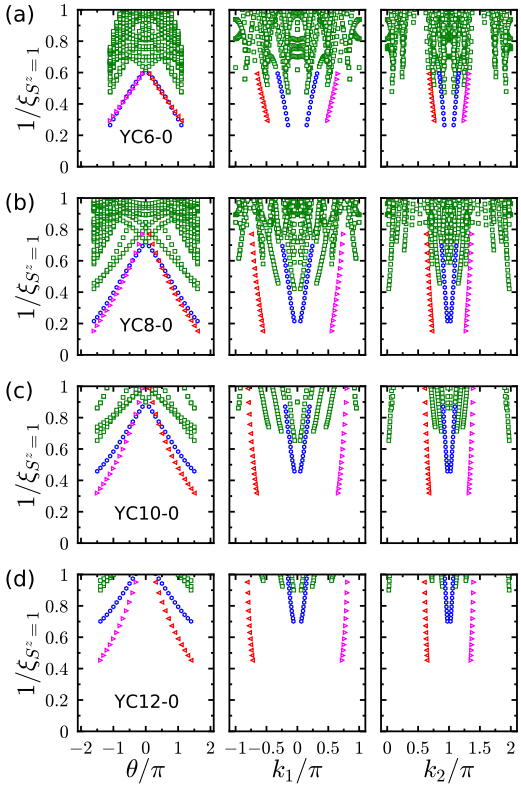

FIG. S6. Inverse of correlation length $1/\xi_{S^z=1}$ (green □) as a function of the flux θ (left column), momentum k_1/π (middle column) and momentum k_2/π (right column) for (a) YC6-0, (b) YC8-0, (c) YC10-0, and (d) YC12-0 cylinders by setting $J_2/J_1 = 0.12$. Bond dimension $m = 6144$ for all cases. Specially, we denote the lowest-lying spinon-pair excitations by blue ⬡, while monopole excitations by red ◁ and magenta ▷. The data is shown for the lowest energy "topological" sector, namely odd sector (sometimes called spinon sector) [6].

YC2n-2k

Next we look at the YC2n-2k cylinder. As we discussed previously, this class of cylinder behaves very different than YC2n-(2k+1) discussed above. For the $U(1)$ Dirac spin liquid, the YC2n-(2k + 1) cylinder hits the gapless Dirac cone at $\theta = \pi$, while YC2n-2k cylinder hits the gapless Dirac cone at $\theta = 2\pi$. Our simulation on the YC2n-2k cylinder is also consistent with this scenario. For YC6-0, the adiabaticity of the twist can be maintained until $\theta = 1.1\pi$, after which the system collapses to the other topological sector. For YC8-0, YC10-0 and YC12-0 cylinders, adiabatic twist can persist until $\theta \approx 1.5\pi$.

Fig. S6 shows the $S^z = 1$ correlation length spectrum of the YC6-0, YC8-0, YC10-0 and YC12-0 cylinders at $J_2/J_1 = 0.12$. We find the lowest modes behave like the fermion bilinears and monopole operators of $U(1)$ DSL. Similar to the YC2n-(2k + 1) cylinder, the lowest modes show a linear dependence with the flux θ. The lowest-lying fermion bilinear appears at $M_2 = (0, \pi)$

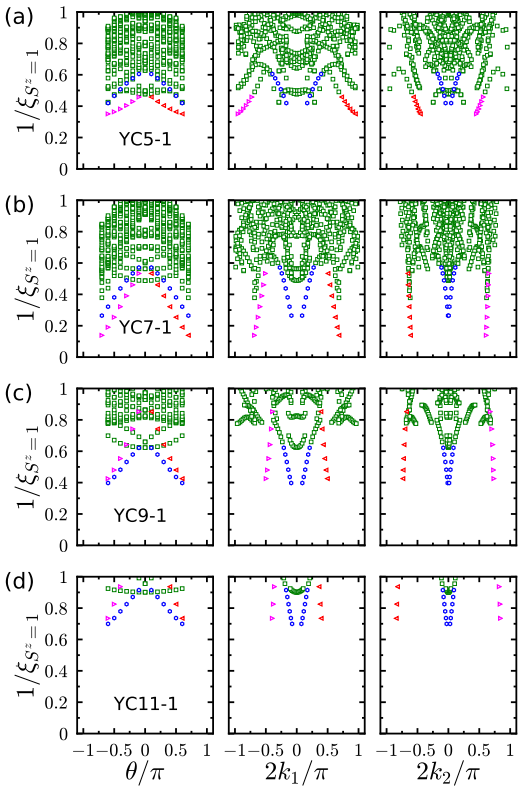

FIG. S7. Inverse of correlation length $1/\xi_{S^z=1}$ (green □) as a function of the flux θ (left column), momentum $2k_1/\pi$ (middle column) and momentum $2k_2/\pi$ (right column) for YCL_y-1 cylinders by setting $J_2/J_1 = 0.12$. Bond dimension (a) $m = 4096$ for $L_y = 5$, (b) 8192 for $L_y = 7$, (c) 6144 for $L_y = 9$, and (d) 4096 for $L_y = 11$ respectively. Specially, we denote the lowest-lying spinon-pair excitations by blue ⬡, while monopole excitations by red ◁ and magenta ▷.

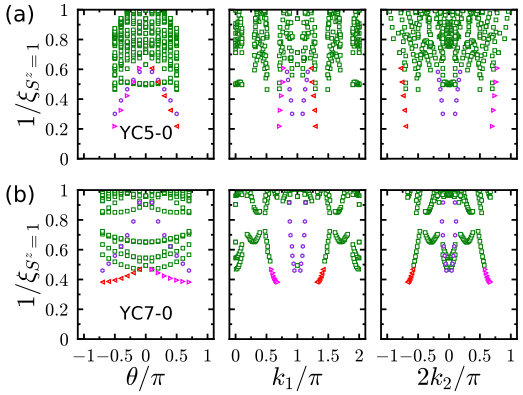

FIG. S8. Inverse of correlation length $1/\xi_{S^z=1}$ (green □) as a function of the flux θ (left column), momentum k_1/π (middle column) and momentum $2k_2/\pi$ (right column) for (a) YC5-0 and (b) YC7-0 cylinders by setting $J_2/J_1 = 0.12$. Bond dimension $m = 2048$ for both cases. Specially, we denote the lowest-lying spinon-pair excitations by violet ⬡, while monopole excitations by red ◁ and magenta ▷.

point (labeled by (k_1, k_2)). We do not find spinon-pair excitations at M_1 and M_3, which can be understood by the explicitly broken rotation symmetry C_6 on a finite-width and infinite-length cylinder. Importantly, we also find that one additional branch appears nearby $K_\pm$ points $(k_1, k_2) = \pm(-2\pi/3, 2\pi/3)$, signaling the expected monopole excitations.

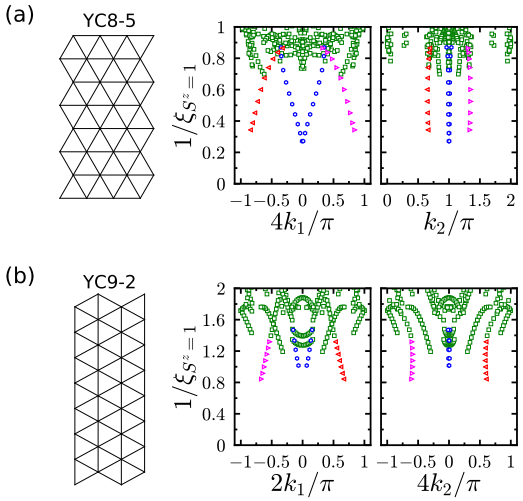

FIG. S9. Inverse of correlation length $1/\xi_{S^z=1}$ (green □) as a function of the momentum k_1/π (middle column) and momentum k_2/π (right column) for geometry (a)YC8-5 (e.g. "XC"8-1 [5]) and (b)YC9-2 ("YC"8-2 [4]) by setting $J_2/J_1 = 0.12$. Bond dimension $m = 4096$ for both cases. Specially, we denote the lowest-lying spinon-pair excitations by blue ⬡, while monopole excitations by red ◁ and magenta ▷.

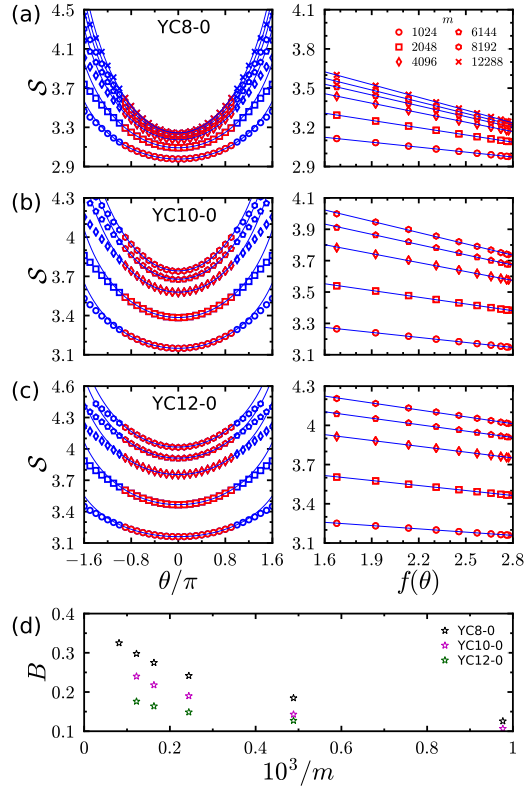

FIG. S10. Entanglement entropy $\mathcal{S}$ as a function of the flux angle θ (left column) and $f(\theta) = \sum_{n=1}^{N_f} \ln|2\sin[s(\theta-\theta_n^c)/2]|$ (right column) for various cylinders: (a) YC8-0, (b) YC10-0 and (c) YC12-0. Bond dimensions $m = 2048$ (□), 4096 (◇), 6144 (⬠), 8192 (⬡) and 12288 (×). We do the fitting of data (red symbols) around minima to the Eq. (2). The best fitting (blue solid line) give us the coefficient B which is marked in the panel (d) as a function of m.

$YC(2n+1)$-$(2k+1)$

Thirdly, the YC$(2n+1)$-$(2k+1)$ cylinder is basically the same as YC$2n$-$(2k+1)$. For the YC$(2n+1)$-$(2k+1)$ cylinder, we expect that spinons hit Dirac cones when $\theta = \pi$ or 3π independent of the emergent gauge flux $\phi = 0$ or π. In Fig. S7, we plot the $S^z = 1$ correlation length spectrum as a function of the flux θ, $2k_1$ and $2k_2$ respectively. Different from YC$2n$-$(2k+1)$ cylinder, the adiabatic twist cannot persist to π due to the small gap and instability of the state as Dirac cone is approached. Furthermore, from the momentum-resolved spectrum we find Fermion bilinears appearing at a M point $(2k_1, 2k_2) = (0, 0)$, and monopoles close to the $K_\pm$ points $(2k_1, 2k_2) = \pm(2\pi/3, -2\pi/3)$.

$YC(2n+1)$-$2k$

In Fig. S8, we plot the $S^z = 1$ correlation length spectrum of YC$(2n+1)$-0 cylinders as a function of the flux θ,

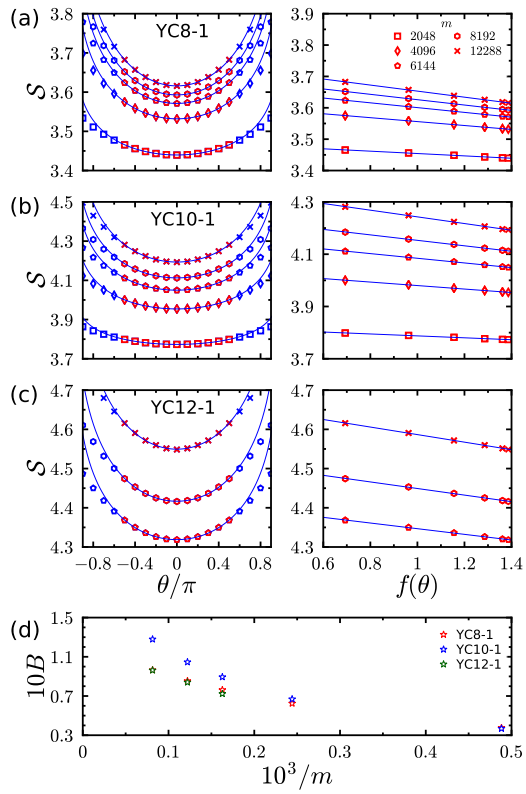

FIG. S11. Entanglement entropy $\mathcal{S}$ as a function of the flux angle θ (left column) and $f(\theta) = \sum_{n=1}^{N_f} \ln|2\sin[s(\theta-\theta_n^c)/2]|$ (right column) for various cylinders: (a) YC8-1, (b) YC10-1 and (c) YC12-1. Bond dimensions $m = 1024$ (○), 2048 (□), 4096 (◇), 6144 (⬠), 8192 (⬡) and 12288 (×). We do the fitting of data (red symbols) around minima to the Eq. (2). The best fitting (blue solid line) give us the coefficient B which is marked in the panel (d) as a function of m.

k_1 and $2k_2$ respectively. We find that the spinon-pair excitations appear at $(k_1, 2k_2) = (\pi, 0)$ (M_1 or M_3 point). Additionally, monopole excitations appears nearby $K_\pm$ $(k_1, 2k_2) = \pm(-2\pi/3, -2\pi/3)$.

Other geometries

In previous studies, people use different geometries, such as "XC" geometry as defined in Ref. [5] (left column of Fig. S9 (a)) and "YC" geometry as defined in Ref. [4] (left column of Fig. S9 (b)). Therefore, we also analyze the adiabatic flux insertion for cylinders "XC"8-1 and "YC"8-2 as shown in Fig. S9.

For the "XC"8-1 cylinder (equivalent to the YC8-5 cylinder), the spinon-pair excitations hit Dirac cones when $\theta = \pi$ independent of the emergent gauge flux $\phi = 0$ or π. In Fig. S9 (a), we find that its Dirac mode appears at a M point $(4k_1, k_2) = (0, \pi)$ modulo 2π. Monopole excitations are very close to $K_\pm$ points $(4k_1, k_2) = \pm(-2\pi/3, 2\pi/3)$.

"YC" cylinders can be transformed to "XC" by a rotation $\pi/2$ in the xy-plane. For the "YC"8-2 cylinder (equivalent to the YC9-2 cylinder), the spinon-pair excitations hit a Dirac cone when $\theta = \pi$ independent of the emergent gauge flux $\phi = 0$ or π too. In Fig. S9 (b), we find that its Dirac mode appears at a M point $(2k_1, 4k_2) = (0, 0)$. Monopole excitations are very close to $K_\pm$ points $(2k_1, 4k_2) = \pm(2\pi/3, 2\pi/3)$ too.

Scaling behavior of entanglement entropy

In addition to Fig. 4, we show more data of entanglement entropy $\mathcal{S}$ for the cylinder YCL_y-0 (Fig. S10) and YCL_y-1 (Fig. S11). Firstly, we find that Eq. (2) accurately fits the data around the minimal value of $\mathcal{S}$ for all the geometries and bond dimensions. Secondly, we notice that the fitting parameter B shows strong dependence on bond dimension, system geometry, etc.. The strong dependence on bond dimension makes it hard to draw a conclusion on the question whether B is a universal quantity or not. However, it is clear that the entanglement entropy always follows the universal scaling law conjectured for the $U(1)$ DSL.

Gaps

Gap measurement

We use an algorithm that combines iDMRG and finite DMRG to calculate the spin gap in Fig. S12. We first obtain a converged wave-function of an infinitely-long cylinder using iDMRG "warm-up" steps. Then we insert a sector of cylinder consisting of $L_y \times L_y$ sites (red cylinder) into the middle of two half-chains. The left (L) and right (R) semi-infinite cylinder can be considered as environment (boundary conditions). We further do sweeps inside the small cylinder and get the lowest energy $E_0(S^z = 1)$ in the $S^z = 1$ sector and the energy of the 1st excited state $E_1(S^z = 0)$ in the $S^z = 0$ sector. Finally, we obtain the gap $\Delta_{S^z=1} = E_0(S^z = 1) - L_y^2 e_0(S^z = 0)$ and $\Delta_{S^z=0} = E_1(S^z = 0) - L_y^2 e_0(S^z = 0)$ where we get the average energy per-site $e_0(S^z = 0)$ during iDMRG calculations.

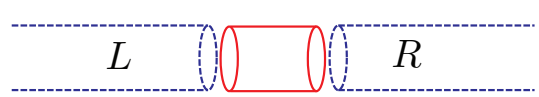

FIG. S12. Schematic picture for the gap measurement in iDMRG.

Gap scaling

In addition to Fig. 2, we show more data for the gap in Fig. S13. For large enough L_y, the spin gap of a DSL at $\theta = 0$ decreases with the circumference size L_y as $\Delta_{S^z=1} \sim v_{S^z=1}/L_y$, but numerically larger L_y also has a larger trunctation error from finite bond dimension m, which tends to overestimate the spin gap in Fig. 2. A simple finite size scaling is therefore difficult, if m sets a larger energy scale. We therefore demonstrate that the gap value becomes lower with increasing truncated bond dimension in Fig. S13, which is consistent with a vanishing gap in the thermodynamic limit ($L_y \to \infty$).

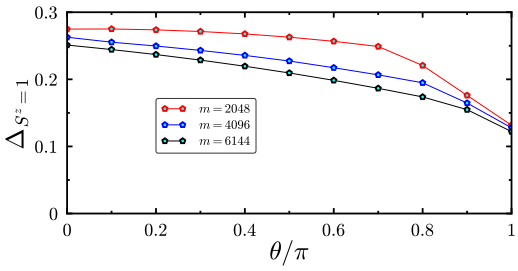

FIG. S13. Dependence of the spin gap $\Delta_{S^z=1}$ (solid line) on the spin flux θ and the truncated bond dimension m. Data is taken with $J_2/J_1 = 0.12$ on the YC10-1 cylinder. Generally the estimated gap decreases with the bond dimension m: For larger the system sizes, the energy scale from truncation becomes relevant, thereby overestimating the spin gap.

* shijiehu@physik.uni-kl.de
† zhuwei@westlake.edu.cn
‡ yinchenhe@perimeterinstitute.ca

[1] Yin-Chen He, Michael P. Zaletel, Masaki Oshikawa, and Frank Pollmann, "Signatures of Dirac Cones in a DMRG Study of the Kagome Heisenberg Model," Phys. Rev. X **7**, 031020 (2017).

[2] V. Zauner, D. Draxler, L. Vanderstraeten, M. Degroote, J. Haegeman, M. M. Rams, V. Stojevic, N. Schuch, and F. Verstraete, "Transfer Matrices and Excitations with Matrix Product States," New Journal of Physics **17**, 053002 (2014), arXiv:1408.5140.

[3] Yin-Chen He, D. N. Sheng, and Yan Chen, "Obtaining topological degenerate ground states by the density matrix renormalization group," Phys. Rev. B **89**, 075110 (2014).

[4] Wen-Jun Hu, Shou-Shu Gong, Wei Zhu, and D. N. Sheng, "Competing spin-liquid states in the spin-$\frac{1}{2}$ Heisenberg model on the triangular lattice," Phys. Rev. B **92**, 140403(R) (2015).

[5] Zhenyue Zhu and Steven R. White, "Spin liquid phase of the $S = 1/2$ J_1-J_2 Heisenberg model on the triangular lattice," Phys. Rev. B **92**, 041105(R) (2015).

[6] S. N. Saadatmand and I. P. McCulloch, "Symmetry fractionalization in the topological phase of the spin-$\frac{1}{2}$ J_1-J_2 triangular Heisenberg model," Phys. Rev. B **94**, 121111(R) (2016).

[7] Shou-Shu Gong, W. Zhu, J.-X. Zhu, D. N. Sheng, and Kun Yang, "Global phase diagram and quantum spin liquids in a spin-$\frac{1}{2}$ triangular antiferromagnet," Phys. Rev. B **96**, 075116 (2017).

[8] Shou-Shu Gong, Wayne Zheng, Mac Lee, Yuan-Ming Lu, and D. N. Sheng, "Gapless Chiral Spin Liquid Phase in Spin-1/2 Triangular Heisenberg Model," arXiv e-prints , arXiv:1905.11560 (2019), arXiv:1905.11560 [cond-mat.str-el].

[9] Frank Pollmann, Subroto Mukerjee, Ari M. Turner, and Joel E. Moore, "Theory of finite-entanglement scaling at one-dimensional quantum critical points," Phys. Rev. Lett. **102**, 255701 (2009).

[10] Wei Zhu, Xiao Chen, Yin-Chen He, and William Witczak-Krempa, "Entanglement signatures of emergent Dirac fermions: Kagome spin liquid and quantum criticality," Science Advances **4**, eaat5535 (2018).